Independent lidar observations support declining low cloud cover trends seen in satellite and reanalysis records

A non-peer-reviewed preprint submitted to EarthArXiv.

Sasu Karttunen*[1,2], Stephan R. de Roode[1], and Angela Meyer[1,2]
[1]Department of Geoscience and Remote Sensing, Delft University of Technology, 2628 CN, Delft, The Netherlands
[2]School of Engineering and Computer Science, Bern University of Applied Sciences, 2502, Biel/Bienne, Switzerland

August 20, 2026

Abstract

Low clouds strongly influence Earth's radiation budget, yet their response to climate change remains uncertain. Recent satellite and reanalysis studies indicate declining low cloud cover that may have contributed to increasing absorbed solar radiation, but independent ground-based evidence over land is limited. Here we show that ground-based lidar observations support a decrease in low cloud cover across mid- to high-latitude land regions. We analyse harmonised 10–25-year records from 16 sites and compare their trends with collocated satellite and reanalysis estimates. Daytime joint trends are significantly negative at the 5% level across datasets, despite considerable variability among sites. Trends are negative at 12–14 of 16 sites across datasets, although their magnitudes differ substantially. Nighttime trends show greater cross-site and cross-dataset variability. Overall, independent lidar observations support the general tendency toward declining low cloud cover indicated by satellite and reanalysis records.

Keywords Cloud cover · Cloud climatology · Climate trends · Remote sensing

1 Introduction

Low clouds strongly modulate the Earth's radiation budget and surface energy balance. Their response to climate change remains a major source of uncertainty in estimates of climate sensitivity, primarily due to the combined contributions of several physical mechanisms that operate on distinct spatial and temporal scales [1; 2; 3; 4; 5; 6]. The total observed change in cloud radiative forcing is a composite of these mechanisms, including temperature-mediated feedbacks, short-timescale adjustments to greenhouse gases, perturbations in aerosol forcing, forced shifts in atmospheric circulation, and coupled land surface–biosphere interactions [7; 5].

The most direct responses to climatic forcing include temperature-mediated feedbacks and rapid adjustments [8; 5; 7]. In marine environments, rising sea surface temperatures drive cloud loss by strengthening the entrainment of dry air from the free troposphere into the boundary layer [9; 10; 11; 12]. Over continental regions, enhanced surface warming typically reduces near-surface relative humidity, a process that suppresses the formation of low clouds [13; 5; 14]. These temperature-driven effects are distinct from rapid adjustments to greenhouse gases, which occur within days of a CO_2 increase and independently of surface warming [15; 8; 5]. For land regions, these include plant physiological forcing, where elevated CO_2 levels cause plant stomata to close partially. This increase in stomatal resistance reduces transpiration, thereby limiting the moisture flux to the boundary layer and further suppressing continental cloud cover [16; 8; 5]. Beyond these thermodynamic effects, forced shifts in the atmospheric general circulation may redistribute cloud regimes geographically. For example, based on analysis of satellite observations, Tselioudis et al. [17] report that a poleward contraction of mid-latitude storm tracks and a widening of the global tropics can replace highly reflective cloud zones with clearer, more absorbent regimes. Simultaneously, recent global reductions in anthropogenic aerosol emissions have weakened the negative aerosol–cloud forcing, effectively warming the climate by decreasing cloud

*s.m.karttunen@tudelft.nl

reflectivity [18; 19; 20]. Over land surfaces, these drivers interact with biosphere–atmosphere coupling, where changes in evapotranspiration and vapour pressure deficit modulate the water supply available for cloud formation [21; 5].

Superimposed with these forced signals is internal climatic variability, which can obscure underlying trends on inter-annual scales [13; 22; 23]. Because the mechanisms influencing clouds range from short-time adjustments to multi-decadal feedbacks, observational and modelling efforts have increasingly focused on partitioning cloud variability over decadal timescales [7; 12; 10; 5]. A decadal (10-30 years) to multi-decadal ($>$ 30 years) perspective is therefore necessary to resolve uncertainties in climate sensitivity, ensuring a sufficient temporal window for emerging forced signals to become detectable while filtering the higher-frequency contribution of natural variability and short-timescale adjustments.

On decadal timescales, satellite observations indicate that recent increases in absorbed solar radiation are primarily driven by a global reduction in low-cloud amount, while the contribution from changes in cloud optical depth remains secondary [7; 24; 17; 9; 12; 25]. Although thermodynamic responses can induce regional increases in cloud optical thickness, most notably in mixed-phase clouds at high latitudes, these effects are largely secondary to the widespread dissipation of low-level cloud cover at the global scale [7; 24]. Consequently, the areal extent of low clouds represents the principal control on the reported decadal acceleration of Earth's energy imbalance (EEI) by low clouds [7; 25].

Recent analyses of global satellite records, notably those from the Clouds and the Earth's Radiant Energy System (CERES) [26] programme, which provides a decadal observational record of Earth's radiation budget and related atmospheric properties, indicate an observable decrease in low-level cloud amount over the last two decades [25; 7; 27; 17]. This decline would lead to an increase in absorbed solar radiation, contributing to the observed decadal acceleration of the EEI [25; 6; 7]. Attributing these trends remains a challenge, as they arise from a composite of underlying mechanisms [7; 6]. While global climate models (GCMs) qualitatively replicate some features of these changes, they often fail to capture the full magnitude of the observed energy imbalance and low-cloud trends. Compared with satellite observations, GCMs systematically underestimate mean-state low-cloud amount while producing clouds that are unrealistically reflective [28; 25; 7; 20; 29; 30]. These discrepancies between models and observations, as well as differences and uncertainties among observational products themselves, require further research on the representation of trends in the underlying datasets [13].

Characterising these trends is complicated by the fundamentally different ways in which fractional low cloud cover (LCC) is represented in and inferred from different observational methods, and reanalyses. Passive satellite instruments adopt a top-down perspective, inferring cloud properties from cloud-top pressure (CTP) observations which are subject to uncertainties arising from obscuration by overlapping upper-level clouds, orbital drifts, and sensor degradation for example [31; 32; 33; 34; 10]. Atmospheric reanalyses, such as ERA5, provide a complementary representation by generating diagnostic cloud fields through prognostic equations constrained by assimilated meteorological observations rather than direct cloud measurements [35]. However, reanalyses are not independent of satellite observations, as satellite measurements are among the data assimilated into them. An independent, ground-up perspective is provided by ground-based remote sensing, such as automatic low-power lidars and ceilometers (ALCs), which provide relatively direct measurements of cloud-base height (CBH) and occurrence [36]. Because these observational and modelling frameworks describe related but non-identical aspects of low-cloud occurrence, inferences regarding decadal change are inherently sensitive to the choice of dataset, cloud definition, and vantage point [37; 3; 38; 6]. While previous investigations have compared individual products or compared them against active-sensor observations, long-term assessments of low-cloud variability have relied primarily on satellite and reanalysis records [39; 40; 41]. Harmonised ground-based remote-sensing records sufficiently long for decadal trend analysis remain scarce. Consequently, direct evidence on whether ground-based remote sensing, satellite-based records, and ERA5 records yield consistent decadal trends remains limited, and without an explicit inter-comparison across these distinct vantage points, any reported agreement or disagreement remains difficult to interpret.

Despite the importance of low-cloud changes for the recent evolution of Earth's energy imbalance, the observational evidence for their long-term change remains difficult to assess independently. Most estimates of decadal low-cloud variability have been derived from satellite observations and reanalyses, which provide broad spatial and temporal coverage but are subject to different sources of uncertainty and are not fully independent: satellite observations contribute to the observations assimilated into reanalyses. Ground-based lidar and ceilometer measurements offer an independent complementary perspective, providing direct observations of cloud occurrence and cloud-base height without relying on the same retrieval framework as passive satellite observations. However, long-term ground-based records suitable for decadal trend analysis remain scarce. Consequently, it remains unclear whether the reported decrease in LCC is consistently reproduced by independent ground-based observations, and whether the magnitude of the change inferred from satellite and reanalysis products is representative of the cloud changes observed near the surface.

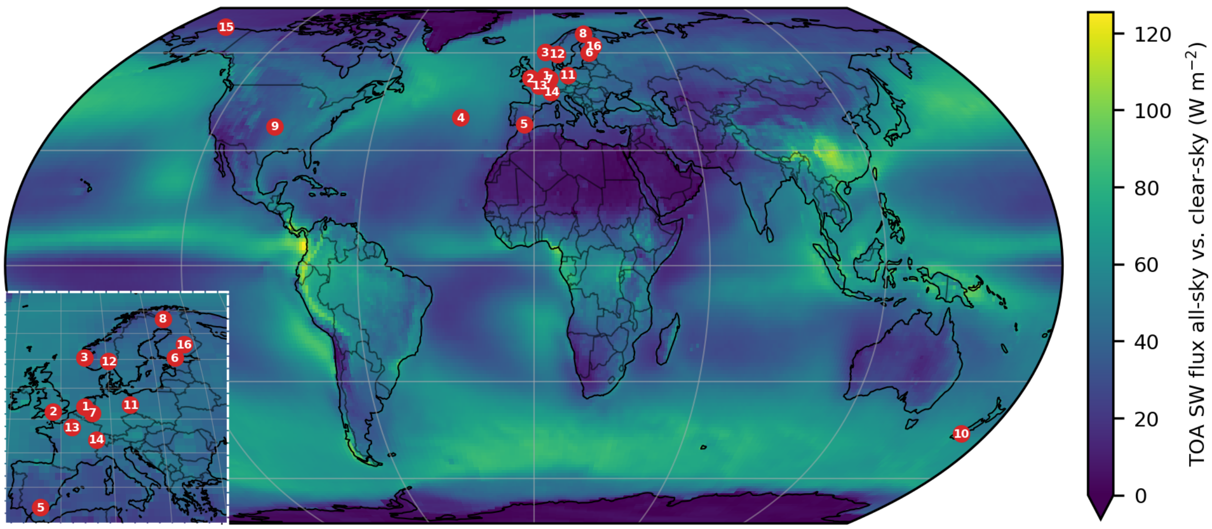

Figure 1: A map of ALC sites included in the study. Also shown is a map of the mean difference in all-sky vs. clear-sky outgoing top-of-the-atmosphere (TOA) shortwave (SW) radiative flux for 2005-2015 using Clouds and the Earth's Radiant Energy System (CERES) satellite analysis. The larger values indicate regions where the clouds have a higher contribution on shortwave radiative budget. The map uses equal-area projection, so the contributions have equal visual weight.

Resolving this gap is important because the magnitude of recent low-cloud changes has direct implications for interpreting the observed increase in EEI. If the decline inferred from satellite observations is representative of changes in low-cloud occurrence over land, it would provide independent evidence for a widespread reduction in a major component of the planetary radiation budget. Conversely, substantial differences between independent estimates would indicate that part of the apparent change depends on how low clouds are detected or represented. Long-term ground-based observations therefore provide an important test of whether the reported decadal reduction in LCC can be reproduced independently of satellite retrievals and reanalysis cloud fields.

To address this, we compile and harmonise 10–25-year ground-based ALC records from 16 sites across mid- to high-latitude land areas (Table 1). Although the sites provide limited global coverage, most are located in regions where clouds make substantial contributions to the net top-of-the-atmosphere shortwave flux at regional and global scales (Fig. 1). We compare the resulting decadal low-cloud trends with collocated CERES and ERA5 estimates over common periods. For ERA5, we calculate LCC using both CBH- and CTP-based definitions to examine whether differences in observational perspective affect the inferred trends. We estimate annual and seasonally resolved trends using a robust non-parametric statistical framework, allowing us to assess the consistency and magnitude of low-cloud changes across ground-based, satellite, and reanalysis datasets.

We show that a predominantly decreasing LCC signal emerges during daytime across the 16 sampled sites in the ALC, ERA5 and CERES records, with joint trends of -1.08 ± 0.58 %-pt dec^{-1} for ALCs, -1.64 ± 0.46 %-pt dec^{-1} for ERA5/CBH, -1.41 ± 0.42 %-pt dec^{-1} for ERA5/CTP, and -1.65 ± 0.38 %-pt dec^{-1} for CERES, all significant at the 5% level. At individual sites, daytime trends are predominantly negative across all datasets, with decreasing trend at 13, 14 and 12 of the 16 sites for ALCs, ERA5 and CERES, respectively. This consistency provides independent ground-based support for recent satellite- and reanalysis-based evidence of declining LCC over mid- to high-latitude land. At night, the joint trends are weaker for ALCs and ERA5 and show greater disagreement between datasets. At individual sites, however, trends are generally less distinguishable from background variability for both daytime and nighttime, highlighting the benefits of analysing an ensemble of sites together. Seasonal analyses further reveal substantial intra-annual variability that is partly obscured by annual averaging.

Table 1: Sites and instruments included in the study. Coordinates and altitudes were taken from the original metadata and should be regarded as approximate.

No	Location	Country	Coordinates	Altitude	Institution	Instruments	References
1	Cabauw	The Netherlands	51.97°N 4.93°E	-1 m	KNMI[a]	LD40, CT75k, CHM15k	[42; 43]
2	Chilbolton	United Kingdom	51.14°N 1.44°W	85 m	STFC[b]	CT75k, CL51	[44; 45]
3	Flesland	Norway	60.29°N 5.22°E	49 m	MET Norway[c]	CHM15k	[46]
4	Graciosa	Portugal	39.09°N, 28.03°W	30 m	ARM[d]	CL31	[47]
5	Granada	Spain	37.16°N 3.61°W	680 m	Univ. of Granada	CHM15k	[48]
6	Jülich	Germany	50.91°N 6.41°E	111 m	Univ. of Cologne	CT25k, CHM15k	[49; 50]
7	Kenttärova	Finland	67.99°N 24.243°E	345 m	FMI[e]	CT25k, CL31	[51; 52]
8	Helsinki	Finland	60.20°N 24.96°E	26 m	FMI	CL51	Not available
9	Lauder	New Zealand	45.04°S 169.68°E	370 m	NIWA[f]	CL31, CL61	Not available
10	Lindenberg	Germany	52.21°N 14.12°E	104 m	DWD[g]	CHM15k	[53]
11	Oslo	Norway	59.57°N 10.43°E	25 m	MET Norway	CHM15k	[46]
12	Palaiseau	France	48.72°N 2.21°E	156 m	IPSL [h]	CL31, CHM15k	[54; 55]
13	Payerne	Switzerland	46.81°N 6.94°E	491 m	MeteoSwiss	CHM15k	[56]
14	Lamont[i]	United States	36.61°N 97.49°W	316 m	ARM	CT25k, CL31	[47]
15	Utqiaġvik[j]	United States	71.32°N 156.61°W	8 m	ARM	CT25k, CL31	[47]
16	Vehmasmäki	Finland	62.74°N 27.54°E	190 m	FMI	CL51	[57]

[a] The Royal Netherlands Meteorological Institute
[b] UK Science and Technology Facilities Council
[c] Norwegian Meteorological Institute
[d] U.S. Department of Energy's Atmospheric Radiation Measurement
[e] Finnish Meteorological Institute
[f] National Institute of Water and Atmospheric Research
[g] Deutscher Wetterdienst
[h] Institute Pierre-Simon Laplace
[i] Central Facility of ARM's Southern Great Plains Observatory.
[j] Central Facility of ARM's Northern Slope of Alaska Observatory.

Table 2: Summary of the temporal coverage of the data used in the analysis, as well as the mean fractional low cloud cover (LCC) for the four datasets. The length is the total record length used in the study, given in fractional years. For ALCs and CERES, coverage is defined as the fraction of valid daily aggregates within the full record length after data extraction, screening, and processing. ERA5 coverage is 100% at all sites. The mean LCCs are computed using the corresponding low cloud definitions associated with the datasets and are therefore not fully comparable. The last three rows indicate the means over the corresponding dataset, giving data from each site an equal weight. These are given separately for all sites as well as mid-latitude and high-latitude sites only.

		Coverage (%)		Mean LCC (%)			
Site	Length	ALC	CERES	ALC	ERA5/ CBH	ERA5/ CTP	CERES
Cabauw	19.7	98.7	96.2	43.2	39.6	36.2	46.0
Chilbolton	23.5	95.6	96.8	48.9	43.9	39.6	53.8
Flesland	11.4	91.8	93.5	53.9	46.5	42.2	63.2
Graciosa	12.3	100.0	93.8	44.1	40.9	35.4	64.4
Granada	11.7	97.1	93.5	14.3	15.0	11.7	22.4
Helsinki	12.2	89.4	93.8	49.7	47.5	44.2	56.8
Jülich	15.2	95.5	95.1	42.9	39.2	35.9	53.1
Kenttärova	17.1	79.8	95.6	43.5	52.3	47.8	56.8
Lamont	24.5	100.0	96.9	17.0	15.9	14.6	26.1
Lauder	10.2	84.8	92.7	25.4	40.1	34.8	45.9
Lindenberg	12.3	100.0	93.9	40.1	36.7	34.9	51.0
Oslo	12.8	99.7	94.2	40.9	34.5	31.8	58.4
Palaiseau	15.1	99.9	95.0	42.9	39.0	36.0	47.5
Payerne	10.3	89.5	92.6	37.6	40.1	33.1	42.9
Utqiaġvik	23.6	96.8	96.8	39.0	76.7	71.9	70.6
Vehmasmäki	10.7	98.0	93.0	54.9	53.9	50.3	61.9
Mean (all)	15.2	94.8	94.6	39.9	41.4	37.5	51.3
Mean (mid-latitude)	14.4	95.7	94.4	39.7	38.1	34.3	49.5
Mean (high-latitude)	20.3	88.3	96.2	41.2	64.5	59.9	63.7

2 Results

2.1 Data coverage and mean LCCs

Table 2 summarises the data-record lengths, data coverage, and mean LCCs for the 16 analysed sites. The start of the CERES record in 2000 limits the record lengths, while ALC-data availability constrains the remaining records. The mean record length is 15.2 years. On average, ALCs and CERES provide valid coverage for 94.8% and 94.6% of the respective record lengths.

2.2 Decadal LCC trends and cross-dataset consistency

The estimated daytime and nighttime decadal LCC trends for the four datasets are shown in Fig. 2, and the corresponding data coverage is summarised in Table 2. For daytime, the joint trends across the sites are -1.08 ± 0.58 %-pt dec^{-1} for ALCs, -1.64 ± 0.46 %-pt dec^{-1} for ERA5/CBH, -1.41 ± 0.42 %-pt dec^{-1} for ERA5/CTP, and -1.65 ± 0.38 %-pt dec^{-1} for CERES. The upper 95% confidence interval bounds are -0.12 %-pt dec^{-1} for ALCs, -0.89 %-pt dec^{-1} for ERA5/CBH, -0.72 %-pt dec^{-1} for ERA5/CTP, and -1.03 %-pt dec^{-1} for CERES. The trends are negative at most sites for all datasets: 13/16 sites for ALCs, 14/16 for ERA5/CBH, 13/16 for ERA5/CTP, and 12/16 for CERES. However, only a minority of the trends for the individual sites are statistically significant at the 5% level: 0/16 for ALCs, 2/16 for ERA5/CBH, 3/16 for ERA5/CTP, and 4/16 for CERES. In addition for CERES, one of the positive trends (that of Chilbolton) is statistically significant at the same level. None of the positive trends in ALC and ERA5 are statistically significant.

The pairwise comparison of the estimated daytime trends in Fig. 3 highlights systematic inconsistencies among the datasets. ERA5 and ALCs show the closest agreement in trend magnitude, with a fitted orthogonal distance regression (ODR) slope of 0.90 ± 0.19, intercept of -0.81 ± 0.28 %-pt dec^{-1}, and a relatively small root mean squared error (RMSE) of 1.29 %-pt dec^{-1}. This suggests a slightly more moderate ALC-observed decrease in LCC compared with ERA5, similarly to the mean values reported earlier, with greater inter-site spread. On the other hand, CERES shows noticeably higher spread between sites compared with ALCs and ERA5, with weaker agreement on trend magnitude (vs.

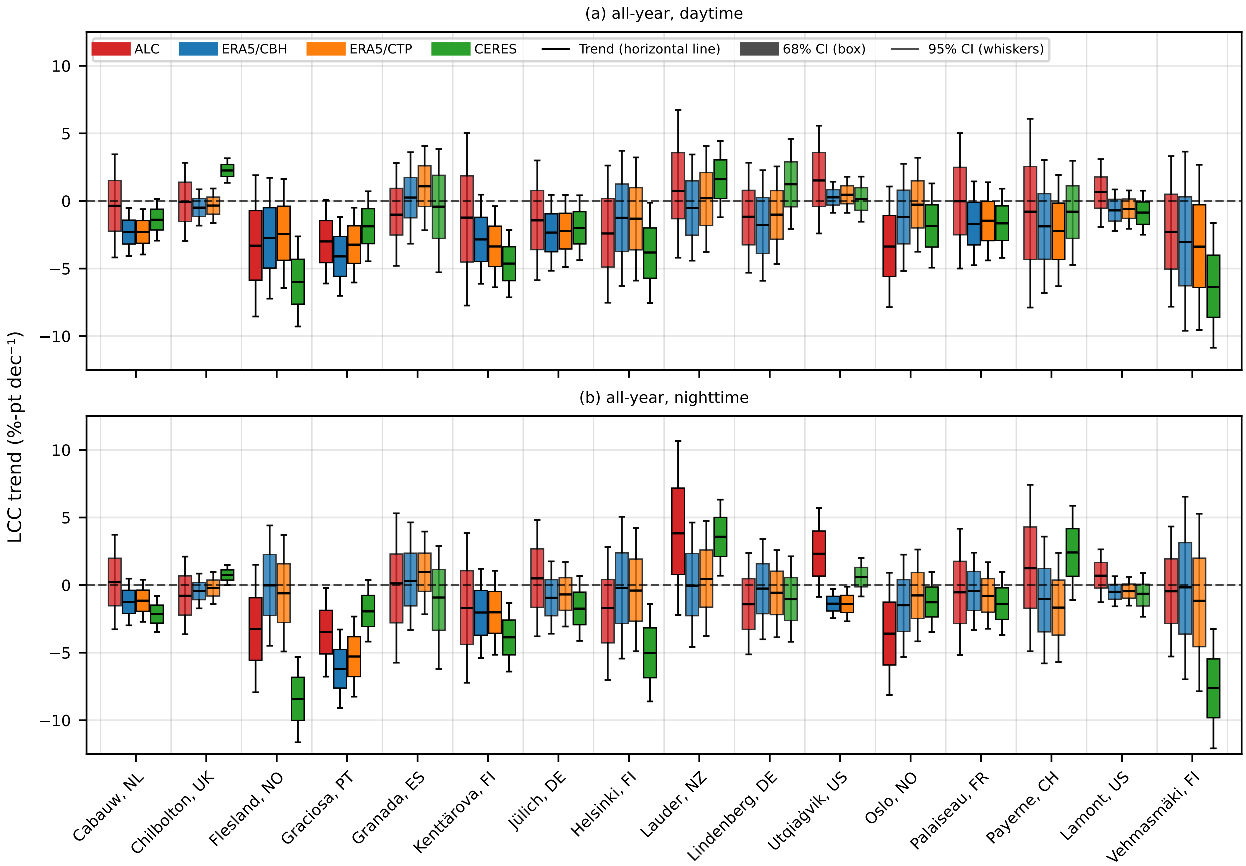

Figure 2: Estimated (a) daytime and (b) nighttime decadal low cloud cover (LCC) trends from ALC, ERA5/CBH, ERA5/CTP and CERES data, describing the estimated LCC trends in the units of percentage points per decade. The trend values are estimated using grouped Theil-Sen estimator, and the associated confidence intervals (CIs) are estimated by inverting the stratified Mann-Kendall test at 68% and 95% confidence levels.

ALC: slope 2.15 ± 0.70, RMSE 1.96 %-pt dec^{-1}; vs. ERA5: slope 2.07 ± 0.52, RMSE 1.82 %-pt dec^{-1}). However, the concordance correlation coefficients (ρ_c) for each cross-dataset comparison is relatively similar, suggesting similar level of general agreement between the datasets.

For nighttime, the joint trends across the sites are -0.51 ± 0.56 %-pt dec^{-1} for ALCs, -1.00 ± 0.47 %-pt dec^{-1} for ERA5/CBH, -0.99 ± 0.42 %-pt dec^{-1} for ERA5/CTP, and -1.81 ± 0.35 %-pt dec^{-1} for CERES. The upper 95% confidence interval bounds are 0.42 %-pt dec^{-1} for ALCs, -0.23 %-pt dec^{-1} for ERA5/CBH, -0.29 %-pt dec^{-1} for ERA5/CTP, and -1.23 %-pt dec^{-1} for CERES. For the individual sites, the trends are less consistent than for daytime: 9/16 sites show negative trends for ALCs, 15/16 for ERA5/CBH, 14/16 for ERA5/CTP, and 12/16 for CERES respectively. Again, only a minority of these are statistically significant at the 5% level: 1/16 for ALCs, 2/16 for ERA5/CBH, 2/16 for ERA5/CTP, and 5/16 for CERES. CERES trend for Lauder is the sole statistically significant positive trend for nighttime across all the datasets.

The pairwise comparison of these nighttime trends in Fig. 4 shows considerably more cross-dataset variability than with daytime. For all cross-dataset comparisons, RMSE and ρ_c indicate weaker agreement than for their daytime counterparts. In ERA5 there is substantially less site-specific variability in the trends compared with ALC and CERES. CERES vs. ALC comparison remains somewhat closer to the daytime equivalent, with $\rho_c = 0.50$ vs 0.54 for daytime.

2.3 Trend seasonality

The seasonally segmented trends show that full-year LCC trends often mask substantial intra-annual variation. At many sites, the annual trend reflects seasonally contrasting changes rather than a uniform year-round decrease, indicating that the decadal evolution of LCC is seasonally structured. This is evident, for example, at the Norwegian sites of

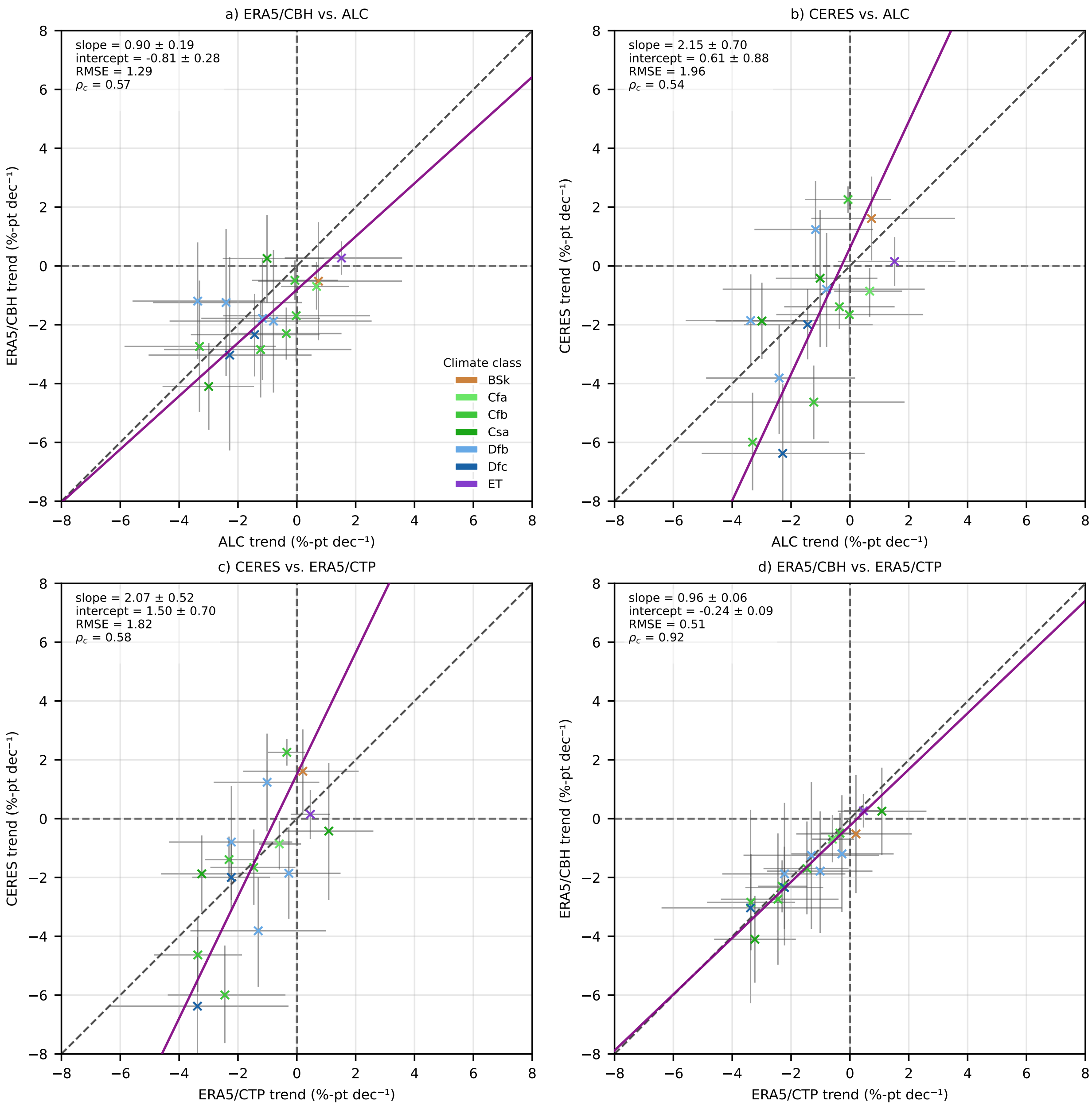

Figure 3: A comparison of decadal daytime fractional low cloud cover (LCC) trends derived from ALC, ERA5/CBH, ERA5/CTP and CERES data. The regression slope is derived from orthogonal distance regression (ODR, purple solid line) using the derived trend uncertainties, with errorbars representing the 68% confidence interval. In addition, mean bias, root mean square difference (RMSD), and concordance correlation coefficient ρ_c are reported as additional statistics.

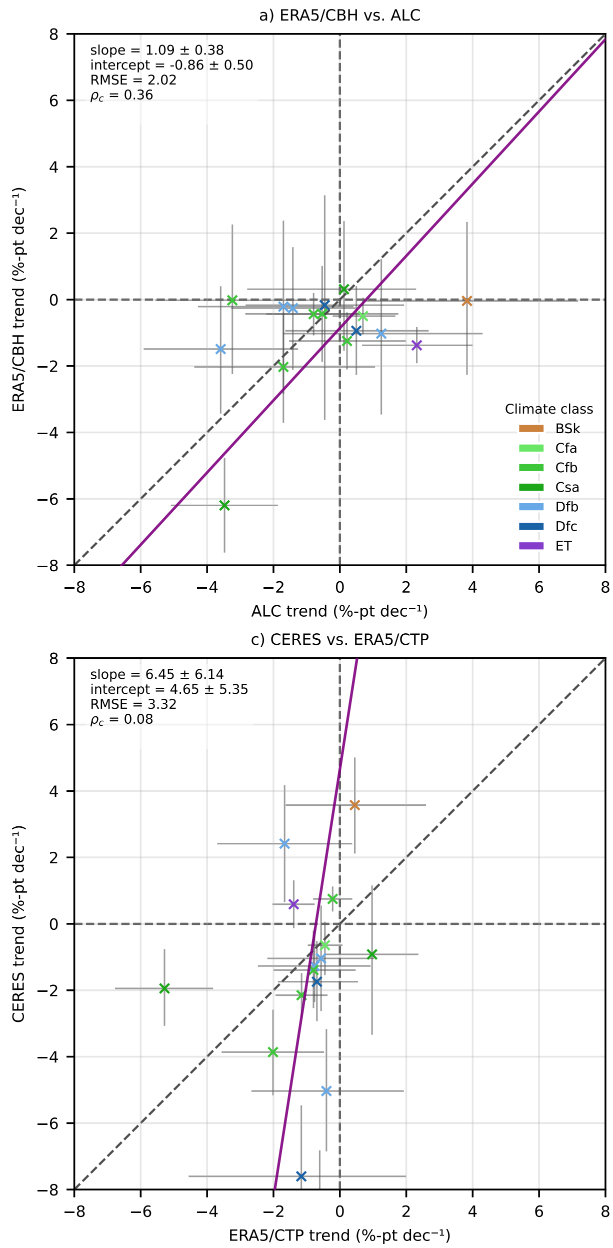

Figure 4: A comparison of decadal nighttime fractional low cloud cover (LCC) trends derived from ALC, ERA5/CBH, ERA5/CTP and CERES data. The regression slope is derived from orthogonal distance regression (ODR, purple solid line) using the derived trend uncertainties, with errorbars representing the 68% confidence interval. In addition, mean bias, root mean square error (RMSE), and concordance correlation coefficient ρ_c are reported as additional statistics.

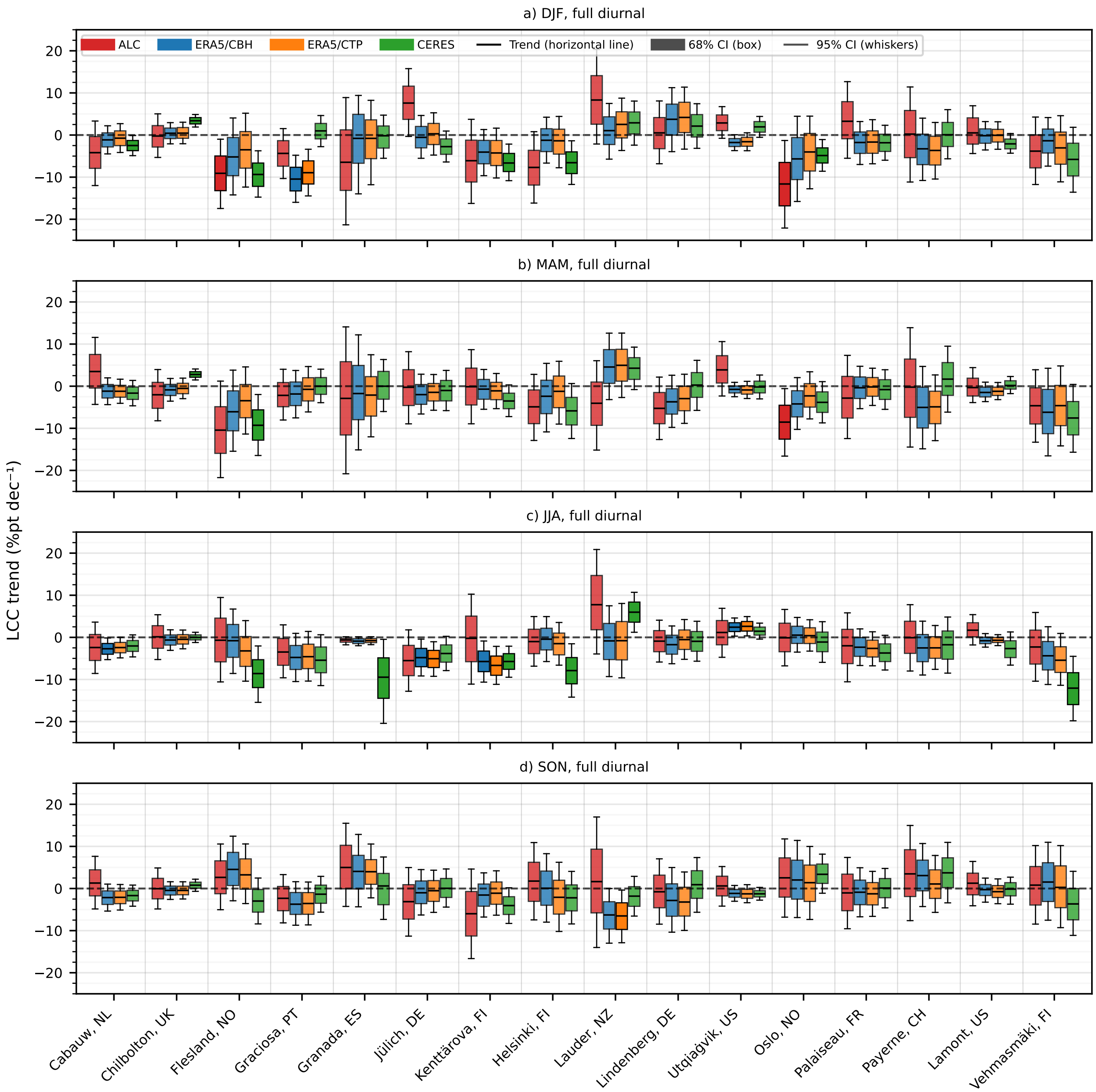

Figure 5: Estimated seasonally segmented decadal trends estimated from ALC, ERA5/CBH, ERA5/CTP and CERES data, describing the estimated LCC trends in the units of percentage points per decade for the meteorological seasons (a-d, December–February DJF, March–May MAM, June–August JJA, and September–November SON). The confidence intervals (CIs) are estimated by inverting the Mann-Kendall test for trend significances at 68% and 95% confidence levels, while the trend values are estimated using grouped Theil-Sen estimator.

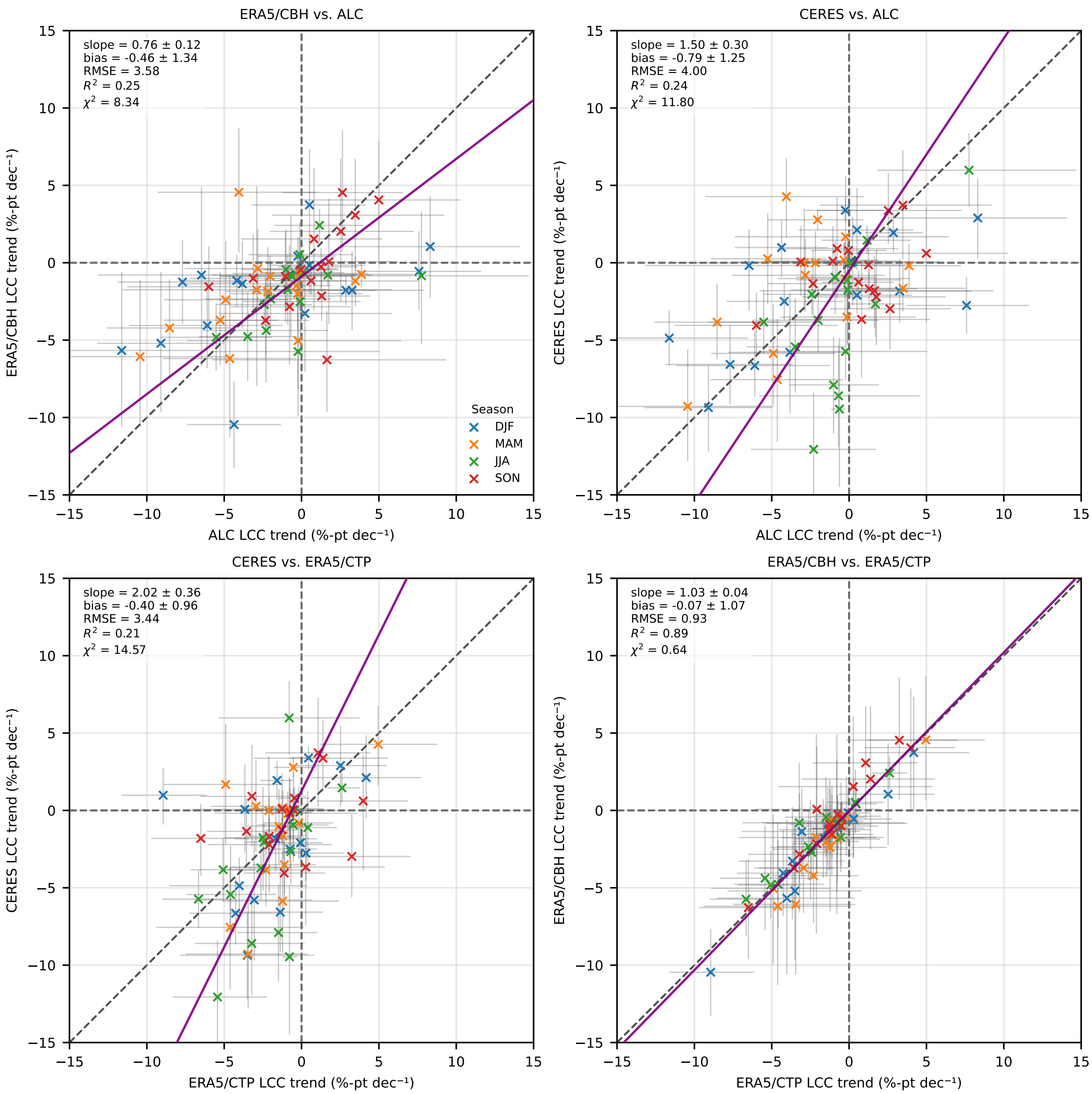

Figure 6: A scatterplot comparison of the seasonally segmented decadal fractional low cloud cover (LCC) trends derived from ALC, ERA5/CBH, ERA5/CTP and CERES data for the meteorological seasons (December–February DJF, March–May MAM, June–August JJA, and September–November SON). The regression slope is derived from orthogonal distance regression (purple solid line) using the derived trend uncertainties, with errorbars representing the 68% confidence interval. In addition, mean bias, root mean square error (RMSE), concordance correlation coefficient ρ_c and χ^2 statistics are reported as additional statistics.

Flesland and Oslo, as well as at Payerne, where negative trends in DJF and MAM coexist with positive trends in SON across more than one dataset. Devasthale et al. [58] similarly reported strong seasonal and spatial heterogeneity in daytime cloud-cover trends over Europe using the CLARA-A3 satellite climate record. Seasonal segmentation therefore provides information beyond the annual trends by identifying when long-term LCC changes are strongest and when compensating seasonal tendencies may obscure the annual signal.

At the same time, the seasonal estimates are less robust than the annual estimates, particularly for ALCs. Seasonal subsampling reduces the number of admissible observations for all datasets, while for ALCs this limitation is compounded by the further stratification of the estimator by instrument. Consequently, the seasonal trends are based on substantially fewer admissible pairwise comparisons and effectively sample relatively few individual seasons, making them more sensitive to subdecadal variability. The larger deviations of individual seasonal ALC trends from ERA5 and CERES should therefore be interpreted cautiously: they may reflect genuine differences in the seasonal behaviour of low clouds but are also more vulnerable to sampling limitations than the corresponding annual estimates. Further targeted seasonal, phase-, and height-resolved analyses would help determine when low-cloud trends are strongest and distinguish changes in cloud occurrence from changes in cloud vertical structure or phase.

3 Discussion

3.1 Representation of low-cloud occurrence

For most sites, ALCs yield mean LCCs that are slightly higher than, or similar to, those from ERA5. However, at the two high-latitude sites, Kenttärova and Utqiaġvik, ALC-derived mean LCCs are substantially lower than the corresponding ERA5 values. This discrepancy may reflect the reduced sensitivity of the ALC retrieval to ice clouds, which are more prevalent at high latitudes. Consequently, optically thin ice clouds represented in ERA5 may not be detected by the ALCs, resulting in lower LCC estimates.

The ALC-derived LCC is also substantially lower than the corresponding ERA5 and CERES estimates at Lauder. This discrepancy is consistent across the two ALC instruments deployed at the site (CL31 and CL61), indicating that it is unlikely to result from an instrument-specific measurement artefact. One plausible explanation is the influence of topography on local cloudiness: the Lauder site is located in the Manuherikia Valley, approximately 10 km from the foothills of the Dunstan Mountains, in the direction of the prevailing westerly winds. The ERA5 and CERES products may therefore represent cloud conditions over both the valley and the surrounding higher terrain.

Compared with ERA5/CTP, CERES-derived mean LCC is higher at all but one site: at Utqiaġvik, the CERES value is 70.6 %-pt, compared with 71.9 %-pt for ERA5/CTP. The mean CERES–ERA5/CTP difference is $+13.8$ %-pt, broadly consistent with the earlier evaluation of SYN1deg products against ground-based observations by Mitra et al. [59], although the magnitude of the difference varies substantially among sites. By contrast, ERA5/CBH is systematically higher than ERA5/CTP, with a mean offset of $+3.8$ %-pt. Thus, changing the ERA5 low-cloud diagnostic produces a comparatively modest and spatially uniform shift in mean LCC, whereas differences between CERES and ERA5/CTP are substantially larger. More generally, passive satellite imagers may overestimate cloud fraction because of finite spatial resolution and subpixel cloud contamination [60].

3.2 Detectability and cross-dataset consistency of LCC trends

On a general level, as represented by negative multi-site daytime joint trends, our results draw a consistent picture of prediominantly decreasing daytime LCC as sampled over our 16 analysis sites. In this sense, the results are broadly consistent with recent large-scale studies reporting declining low-cloud amount in recent decades [e.g. 7; 25; 6] that rely on satellite and reanalysis estimates. The ALC estimate has a slightly higher uncertainty than those of ERA5 and CERES, resulting from the use of a stratified estimator that excludes cross-instrument comparisons. This in turn reduces the number of admissible three-day observation pairs at sites where the observations come from multiple instruments, widening the confidence intervals. Despite this, all of the joint daytime trends are statistically significant at the 5% level, including the ALC estimate.

At the level of individual sites, however, the picture is less consistent; some sites show broadly consistent behaviour across datasets, whereas others exhibit substantial differences in trend magnitude and, in some cases, trend sign. Considerable discrepancies include stronger negative trends in CERES compared with Flesland, Kenttärova, Helsinki, and Vehmasmäki, all higher mid-latitude sites. Conversely, for Cabauw, Kenttärova, Jülich, Utqiaġvik, Palaiseau, and Lamont, the ALC-derived trends show an apparent positive bias relative to both CERES and ERA5. For most of the individual sites across all datasets, the trend signal is not negative at 5% significance level. This indicates that the decadal signal is both spatially heterogeneous and only partially distinguishable from background variability at single sites and the record lengths analysed here.

Also during the nighttime, the joint trends indicate a predominantly decreasing LCC. The picture is however less clear than in daytime, as the ALC trend is not significant at the 5% level. The cross-dataset comparisons indicate that nighttime is also associated with much stronger discrepancies between ALCs, ERA5 and CERES. Nighttime conditions tend to place greater emphasis on fog and very low-level clouds, which can be difficult to represent consistently across observing systems. Although direct prior evaluations over land are lacking, comparisons against ship-based lidar measurements over oceanic regions indicate that ERA5 can substantially underestimate fog and very low-level cloud occurrence [61]. At the same time, cloud detection using passive satellite radiometers becomes more uncertain at night due to lack of visible-channel and the weaker thermal contrast between cloud tops and the surface [62]. Conversely, the signal-to-noise ratio of the ALC backscatter actually improves during nighttime due to absence of solar radiation [63; 64]. These factors provide a plausible explanations for why cross-dataset correspondence is weaker at night, although the present analysis cannot separate their relative contributions. Although nighttime trends lack influence on the shortwave radiative balance, they may still affect EEI by altering the longwave cloud greenhouse effect. Hence, quantifying and understanding the nighttime trends and the observed differences across datasets warrants further research.

These findings have implications for the broader interpretation of recent low-cloud changes. They provide independent land-based support for the sign of the decadal low-cloud tendency inferred from satellite and reanalysis studies: over 16 mid- to high-latitude land sites, the observed change is more consistent with decreasing than increasing LCC, especially during daytime. Our findings are qualitatively consistent with the idea that low-cloud reductions could contribute to the recent intensification of Earth's energy imbalance by reducing planetary shortwave reflection [7; 25; 6].

An open question remains whether the weaker joint trends indicated by ALCs compared with ERA5 and especially CERES are more reflective of the ground truth than these stronger trends. One candidate explanation for the weaker negative trends in the ALC records would be the reduced sensitivity of ALC retrievals to ice clouds. This could make ALC-derived trends sensitive to changes in the phase composition of low clouds, for example, if low-level ice clouds are replaced by liquid and mixed-phase clouds in a warming climate. Although this effect is expected to be negligible at most sites because low-level ice clouds are infrequent, it could induce a positive trend bias at higher-latitude sites. However, the positive ALC biases compared with ERA5 and CERES are not exclusive to high-latitude sites. Furthermore, CERES could have a similar underlying bias with respect to changes in phase composition, because the underlying passive satellite imagers detect optically thick liquid cloud layers more robustly than optically thin ice clouds [65]. This suggests that phase changes do not fully explain the observed positive trend bias relative to the other two datasets.

Conversely, a true negative bias in CERES trends could at least partially explain why low-cloud feedback is underestimated in Coupled Model Intercomparison Project (CMIP) Phase 5 and 6 climate model simulations relative to satellite-based estimates, as reported by Ceppi et al. [28]. If such a bias were to arise from the underlying satellite observations, it could potentially also propagate into ERA5 through data assimilation. However, climate model estimates provide no more than weak support for a negative LCC trend bias in CERES, given the inherent uncertainties associated with them, with differences in retrieval characteristics being a more likely explanation. The underlying reason why ALC records suggest weaker negative trends than ERA5 and CERES remains unresolved in our analysis.

The diagnosed low-cloud fraction depends not only on changes in cloud occurrence, but also on changes in cloud vertical structure relative to the adopted classification boundary [37; 3]. With the non-obscured CTP-based definition, changes in cloud-top height, thickness of the low-tropospheric atmosphere, or vertical overlap can alter the diagnosed trends without equivalent changes in boundary-layer cloud occurrence. A similar issue applies to the ground-up products used here: if cloud-base height shifts relative to the fixed height threshold, the diagnosed low-cloud fraction can change without an equivalent change in overall cloud occurrence. Such structural sensitivities could contribute to cross-dataset differences between satellite- and ground-based records. However, the ERA5/CBH vs. ERA5/CTP ODR slope and intercept fall well within the estimated aleatoric uncertainty of the trend estimates,

3.3 Limitations

The compiled 10–25-year ALC dataset provides a decadal-scale, ground-based record of LCC observations across several climate zones, enabling an independent assessment of low-cloud trends from direct measurements, complementary to satellite estimates and reanalysis. However, the record is limited to 16 sites, most of which are located in the Northern Hemisphere, which hinders the global generalisability of the results. As reported based on CLARA-A3 satellite climate record by Devasthale et al. [58], the cloud cover may also exhibit strong regional heterogeneity. Such heterogeneities can also weaken the correspondence of ALC-type point measurements compared with grid-cell averages of ERA5 and CERES. Furthermore, especially for individual sites separately, extracting the underlying decadal trends from these relatively short records remains challenging as the observed LCC variability reflects a superposition of internal climate variability, synoptic to interannual variability, and other shorter-timescale fluctuations.

Although ALCs can operate reliably for extended periods without maintenance [66], their reliance on fixed installation platforms and occasional maintenance access limits their deployment over open oceans and in other remote regions over longer periods of time. ALCs can be deployed aboard ships to observe maritime clouds [e.g. 67; 68; 61], but obtaining frequent, spatially consistent, long-term observations remains challenging. In dust-affected environments, the instruments also require more frequent manual cleaning to maintain sufficient optical transmission [69]. These constraints, together with the costs of establishing a dense global network, limit the spatiotemporal coverage of ALC-based cloud observations. Extending the present analysis will therefore require long-term observations in poorly represented regimes, particularly over open oceans and other remote regions where persistent low-cloud decks are climatically important. Shipborne ALC deployments, new active-sensor missions such as EarthCARE [70], and newer passive imagers may help reduce this sampling gap, but they do not replace the need for a geographically broader long-term reference network. Our study also underscores the need to maintain and expand long-term ground-based cloud-observing networks to independently constrain low-cloud changes, which remain a major source of uncertainty in climate projections.

CERES SYN1deg product is designed as a temporally consistent climate data record, but its underlying cloud retrievals and temporal sampling nevertheless rely on an evolving constellation of polar-orbiting and geostationary imagers. The polar-orbiting observations transitioned from Moderate Resolution Imaging Spectroradiometer (MODIS) observations from Terra satellite alone to combined Terra and Aqua MODIS observations and, more recently, to include Visible Infrared Imaging Radiometer Suite (VIIRS) observations from NOAA-20 satellite and the contributing geostationary have sensors also evolved. Geostationary observations provide the frequent temporal sampling needed to characterise the diurnal cycle between the relatively infrequent polar-orbiting and CERES observations, while the CERES processing system harmonises the contributing observations and applies radiative-consistency constraints. Residual inhomogeneities associated with changes in the observing system therefore cannot be completely excluded [71; 72; 73]. Despite the constraints, CERES data is affected by the intrinsic limitations of passive satellite cloud retrievals and their sampling, including uncertainties in cloud-top pressure under strong temperature inversions, obscuration of low clouds by overlying clouds, and viewing-angle and orbital-drift effects [74; 40; 75; 76]. These effects may therefore contribute to persistent differences between the datasets and, where their magnitude changes over time, to differences in LCC trends. The same limitations and biases in satellite retrievals may partially propagate into ERA5 as well through its data assimilation system, for the same reason ERA5 and satellite records should not be considered completely independent data sources.

Despite the more direct nature of ALC cloud observations through active retrieval when compared with passive radiometers, they are not guaranteed to be free of measurement errors either. In addition to limitations of ALCs with respect to observing ice clouds discussed earlier, the retrieval performance of the instruments can change over time. Although the cloud detection algorithm we used is robust against calibration drifts, there is no guarantee that this also holds for other factors that might deteriorate the signal, such as heavy window contamination or instrument malfunctions. We used the best available information to exclude data affected by identified defects, based on, for example, measurement logs and instrument diagnostics where available. However, the completeness of these records is something that we cannot ensure. Instead of selecting best available data, we opted for better temporal and geographical coverage, aiming for best available joint trend estimates using statistical techniques robust to outliers. At the same time, it cannot be ruled out that especially the trends from individual sites may be affected by unknown factors affecting the retrieval performance.

Finally, although LCC is directly linked to Earth's radiation budget, the present analysis does not permit a quantitative estimate of the contribution of LCC changes to EEI from ground-based observations. This limitation arises from the restricted global coverage and the absence of corresponding radiative-flux measurements. Moreover, the radiative effect of a given LCC change depends on other cloud properties, including cloud optical thickness, thermodynamic phase, and cloud-top height, as well as the underlying surface state. Consequently, a change in LCC alone cannot be directly translated into a change in Earth's radiation budget or a contribution to global EEI. Nevertheless, the independent evidence of LCC changes provided by ground-based observations can help constrain the cloud changes that contribute to variations in Earth's radiation budget.

4 Methods

4.1 Automatic low-power lidars and ceilometers (ALCs)

The core of the dataset is based on ALC measurements from Aerosol, Clouds and Trace Gases Research Infrastructure (ACTRIS) Cloudnet [36; 77] and the U.S. Department of Energy Atmospheric Radiation Measurement (ARM) [78] user facility, covering eight and three sites across Europe and North America, respectively. In addition, we include ALC measurement data acquired from open repositories (four sites, of which two are Cloudnet sites) and through private

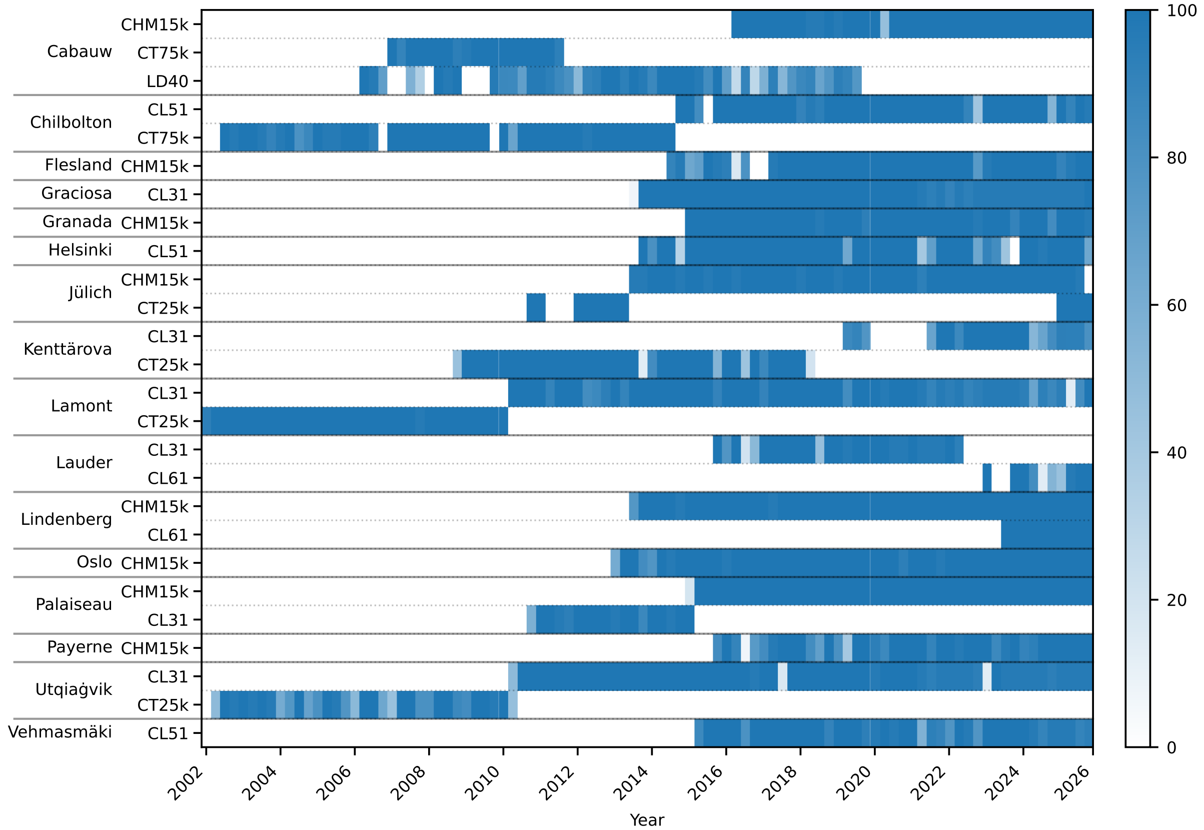

Figure 7: Temporal coverage of ALC data available for the trend analysis after screening and post-processing.

communication (five sites, of which two extend data coverage from a Cloudnet site). Our two criteria for site selection were: a coverage of valid ALC data of at least 10 years up to 2025, and availability of the original raw attenuated backscatter coefficient profiles, from one or multiple instruments. The first criterion was considered a minimum for decadal trend analysis, and the second one was necessary for application of a consistent post-processing and LCC estimation across all sites and instruments. The collected dataset contains data from seven different instrument models: LD40, CT25k, CT75k, CL31, CL51, CL61 (Vaisala Oyj, Finland), and CHM15k (G. Lufft Mess- und Regeltechnik GmbH, Germany until 2016; OTT HydroMet GmbH, Germany from 2016).

Based on Köppen–Geiger climate classification maps by Beck et al. [79], five of the analysed sites represent marine humid winter (Cfb; Cabauw, Chilbolton, Flesland, Jülich, and Palaiseau), four warm-summer humid continental (Dfb; Helsinki, Lindenberg, Oslo, and Payerne), two hot-summer Mediterranean (Csa; Graciosa, Granada), and two subarctic (Dfc; Kenttärova, Vehmasmäki) climates. Furthermore, cold semi-arid (BSk; Lauder), humid subtropical (Cfa; Lamont), and tundra (ET; Utqiaġvik) climates are represented by one site each. Out of the 16 sites, seven (Cabauw, Chilbolton, Flesland, Graciosa, Helsinki, Utqiaġvik, and Oslo) can be considered coastal as they are located within 50 km of the nearest coastline, with the remaining nine being located further inland.

The starting point of processing of our ALC datasets was the raw attenuated backscatter profiles as a function of height and time. We processed these raw backscatter profiles following the processing scheme used by Cloudnet for ALCs [36; 80], with the addition of a near-range correction for the LD40 instrument [81]. The Cloudnet processing scheme implements post-processing of raw backscatter signals from a range of different ALC instrument models into denoised backscatter profiles for further analysis. Instead of relying on instrument-reported cloud detection, we reprocessed all raw backscatter profiles using the Cloudnet scheme to ensure consistent retrieval methodology applied throughout ALC dataset. Prior to any processing, the data was roughly screened for immediately obvious issues based on measurement logs, diagnostics reported by the instruments (where available), and other clear anomalies.

To calibrate the source backscatter profiles, we used default instrument-specific calibration coefficients from Cloudnet. As the cloud detection algorithm we used in downstream processing is only weakly dependent on calibration, this accuracy in the calibration can be considered sufficient for the purpose. Nevertheless, we explored the sensitivity of ALC-derived LCC trends to calibration further using sensitivity tests. According to the tests, artificially imposed $\pm 20\%\ \mathrm{dec}^{-1}$ calibration drifts can induce biases in the LCC trends of up to $3.4 \times 10^{-2}\ \% - \mathrm{pt\ dec}^{-1}$. The corresponding aleatoric uncertainties for the derived trends were at least 85 times larger than the resulting trend biases in all cases, demonstrating the weak dependence of the processing on calibration.

To derive LCC from the backscatter data, we utilised the algorithm by Tuononen et al.[80]. The algorithm identifies liquid cloud layers from the calibrated and noise-screened backscatter profiles, which is also used by Cloudnet. However, in the Cloudnet implementation as part of the CloudnetPy package [82], the algorithm is embedded into a comprehensive classification scheme that also utilises cloud radar, microwave radiometer and ECMWF (European Centre for Medium-Range Weather Forecasts) Integrated Forecasting System (IFS) model data beyond the lidar backscatter profiles. As the cloud radar and microwave radiometer datasets are not available for a majority of the ALC data presented in the present study, we wrote and used a lidar-only reimplementation of this algorithm following the up-to-date CloudnetPy version instead.

An important advantage of the algorithm is that it is not instrument-specific and depends only weakly on calibration. It can therefore be applied consistently across different ALC models without instrument-specific parameter tuning, which is particularly important here because the dataset includes instruments from multiple manufacturers. For the same reason, we did not use instrument-reported CBHs for low-cloud detection, as these rely on manufacturer-specific algorithms that can differ substantially between models. These algorithms are also often proprietary, not openly documented, and may be sensitive to calibration.

The current algorithm is an extension of an earlier Cloudnet algorithm [36]. Unlike the original algorithm, instead of relying on a global attenuated backscatter threshold value for finding peaks in the backscatter caused by liquid layers, it uses a localised peak search and additional criteria for the peak width and shape. This decreases the algorithm's sensitivity to calibration and other factors affecting the retrieval performance, as well as makes it possible to discriminate between cloud layers, precipitation and fog. The algorithm is generally sensitive to cloud layers with liquid droplets, including mixed-phase clouds to some extent. However, it is not sensitive to weakly-attenuating ice clouds, which are more difficult to distinguish from background noise in ALC backscatter profiles. Using the resulting binary cloud masks, we computed ALC-derived LCC ($f_{\mathrm{low|liquid}}$) as the fraction of time within a given aggregation period (e.g. 1 h) for which cloud layers were detected below 2 km a.g.l.

To give an impression of the ALC data in practice at subdaily scale, Fig. 8 shows a single example of backscatter and derived LCC from three sites in Western Europe (Cabauw, Chilbolton, and Jülich) on 2017-02-28, along with a comparison to ERA5- and CERES-derived LCC at hourly time scale.

4.2 CERES

As the satellite-based record, we used the CERES Synoptic TOA and Surface Fluxes and Clouds (SYN1deg) Edition 4.2 hourly product [71; 72]. This product provides mean cloud and radiative properties on a global $1^\circ \times 1^\circ$ latitude–longitude grid from March 2000 onwards. SYN1deg combines cloud retrievals from multiple polar-orbiting and geostationary satellite imagers to produce temporally complete global cloud fields. Within the CERES processing system, retrieved cloud and atmospheric properties are adjusted within their estimated uncertainties to ensure that radiative-transfer calculations are consistent with observed CERES top-of-the-atmosphere broadband radiative fluxes, yielding a radiatively consistent cloud-property dataset. We selected SYN1deg because it provides a long-term daily climate data record developed for climate applications. The cloud properties retrieved within the CERES processing system are also used to derive the cloud radiative effects reported in the Energy Balanced and Filled (EBAF) [83; 84] product, which is widely used in studies of EEI, radiative forcing, and cloud radiative effects.

Clouds in SYN1deg are classified according to the International Satellite Cloud Climatology Project (ISCCP) [85] scheme, which separates cloud layers by CTP [86]. Low clouds are defined as those with $\mathrm{CTP} \geq 680\ \mathrm{hPa}$, corresponding to a cloud-top height of approximately 3.2 km a.s.l. in the standard atmosphere. This top-down definition differs fundamentally from the ground-based ALC definition, which identifies low clouds according to cloud-base height (CBH). Consequently, satellite-derived low-cloud fractions represent only the portion of the low-cloud field visible from above, while optically thick overlying clouds may obscure underlying low clouds. Likewise, vertically deep clouds with low cloud bases but cloud tops above the CTP threshold are not classified as low clouds. These differences arise from both the observing geometry and cloud-classification methodology. Nevertheless, provided that these systematic differences remain broadly stable over time, temporal variability and long-term trends derived from satellite and ground-based observations can be compared.

For the trend analysis, we extracted the daily cloud record from the SYN1deg grid cell encompassing each observation site using nearest-neighbour selection. We used the adjusted cloud fractions provided by SYN1deg. To reduce sensitivity

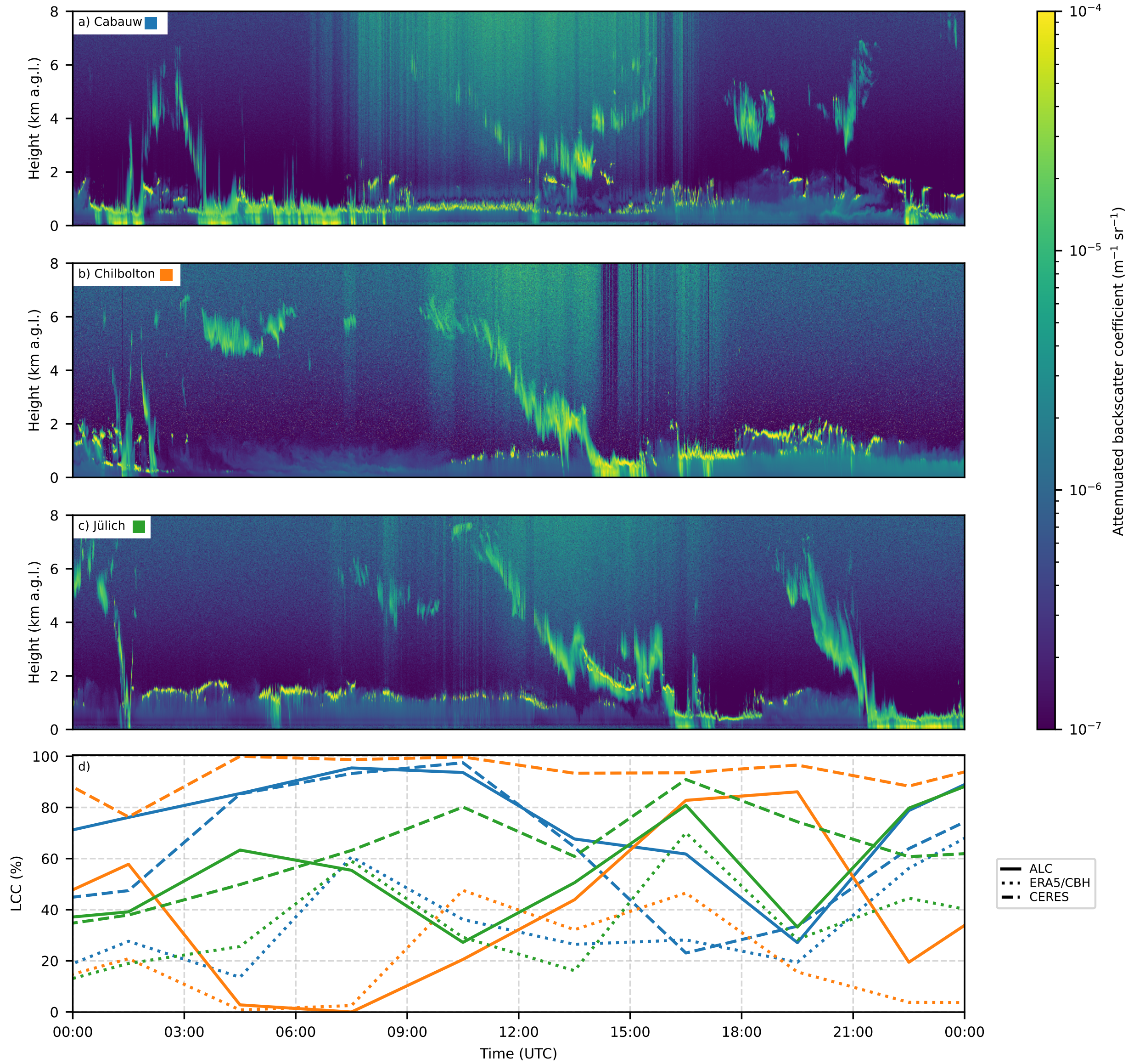

Figure 8: The ALC-measured attenuated backscatter coefficient from Cabauw, Chilbolton, and Jülich on 2017-02-28 as function of time and height a.g.l. (a-c). The derived fractional LCC, along with the ERA5/CBH and CERES counterparts are presented in the bottommost panel (d), the colors are indicated next to the site names in panels (a-c). The time series in panel (d) are downsampled into three-hour averages for clarity.

to temporal variations in the obscuration of low clouds by higher cloud layers, we analysed the unobscured low-cloud fraction rather than the total low-cloud fraction. Following Scott et al. [10], the unobscured low-cloud fraction is defined as

$$f_{\mathrm{low|visible}} = \frac{f_{\mathrm{low}}}{1 - f_{\mathrm{tot}} + f_{\mathrm{low}}}, \tag{1}$$

where f_{low} and f_{tot} denote the adjusted low- and total-cloud fractions reported by SYN1deg. This metric represents the fraction of sky not covered by higher clouds that is occupied by low clouds and is therefore less sensitive to temporal variations in cloud overlap. Assuming that obscured and unobscured low clouds evolve similarly over time, $f_{\mathrm{low|visible}}$ has been widely adopted as a proxy for changes in total low-cloud cover in observational studies of low-cloud trends and cloud feedbacks [10; 87; 88].

4.3 ERA5

ERA5 is ECMWF's latest global reanalysis produced by the Copernicus Climate Change Service and ECMWF [35]. It provides a record of the global atmosphere, land surface and ocean waves from 1950 onwards at substantially higher spatial and temporal resolution than earlier-generation ERA-Interim, with a native horizontal resolution of approximately 31 km. ERA5 also includes an ensemble-based uncertainty estimate at reduced resolution, although only the deterministic reanalysis is used here.

ERA5 is produced using ECMWF IFS version CY41R2 for data assimilation and atmospheric forecasting. In IFS, clouds are represented as fractional cloud cover on individual model levels. For diagnostic output and radiative transfer calculations, vertically aggregated cloud cover is then computed from these model-level cloud fractions using an exponential-random overlap model [89; 90; 91]. In the ERA5 dataset and ECMWF forecasts, the resulting total, low, medium and high cloud cover diagnostics are archived as standard output variables. The default ERA5 LCC diagnostic (parameter identifier 186) is defined over all cloud layers between the surface and 0.8 times the surface pressure. The cloud cover on model levels is represented as a sum of spherical harmonics, which can be transformed into native reduced Gaussian grid of ERA5 (N320, where 320 refers to the number of quadrature points along a meridian between the pole and the equator) using discrete Legendre transform. The cells in the N320 grid are roughly uniform in size, with an approximate area between 900 km^2 and 1000 km^2. The ERA5 reanalysis is available at hourly temporal resolution, with analyses twice a day at 06 and 18 UTC, bridged with forecasts.

This default ERA5 LCC diagnostic is not directly comparable to either ALC- or satellite-derived LCC because the underlying definitions differ. Relative to ALCs, the main differences arise from the use of pressure-referenced rather than geometric-height cloud layers and from the inclusion of all cloud phases in the archived diagnostic. Relative to passive satellite observations, the main differences arise from the top-down point-of-view and classification of clouds by their CTP. In a comparative study, using the archived ERA5 diagnostic alone would therefore combine differences introduced by the diagnostic definition itself with differences in the underlying temporal variability of the cloud field represented by each data source. To reduce this ambiguity, we derived two comparison-specific ERA5 products from original hourly N320 grid model-level data: one matched to the CBH-based and one matched to the CTP-based definition.

For the comparison with ALCs, we recomputed LCC using model surface and 2 km a.g.l. geometric height as the lower and upper bounds for low-cloud CBH, respectively. The 2 km upper bound follows the World Meteorological Organization's International Cloud Atlas definition. This choice therefore follows the ALC definition more closely than the default ERA5 diagnostic, which is referenced to fraction of surface pressure rather than geometric height, we refer to this product as ERA5/CBH for the remainder of the paper. Using the exponential-random model, the overlap between cloud covers C_k and C_l at model levels k and l as a linear combination of maximum and random overlap:

$$C_{k,l} = \alpha_{k,l} C_{k,l}^{\mathrm{max}} + (1 - \alpha_{k,l})\, C_{k,l}^{\mathrm{ran}}, \tag{2}$$

where $C_{k,l}^{\mathrm{max}}$ is the maximum possible overlap

$$C_{k,l}^{\mathrm{max}} = \max\left(C_k, C_l\right), \tag{3}$$

and $C_{k,l}^{\mathrm{ran}}$ is the random overlap

$$C_{k,l}^{\mathrm{ran}} = C_k + C_l - C_k C_l. \tag{4}$$

The factor for linear combination $\alpha_{k,l}$ is defined based on the vertical distance between the two levels $\Delta z_{k,l}$ and decorrelation length $z_0(\phi)$ [91]: $\alpha_{k,l} = \exp\left(-\frac{\Delta z_{k,l}}{z_0}\right)$,

$z_0 = a + b\cos^2\phi$ where $a = 7.5 \times 10^2$ m and $b = 2.149 \times 10^3$ m are empirical constants based on cloud radar campaigns, and ϕ is the latitude. The height-dependent cloud fraction can then be derived by cumulatively applying the cloud overlap model repeatedly over the model levels within the desired height range. The resulting cloud fraction represents the spatial proportion of a N320 grid cell covered by clouds in these levels at the given analysis time. For each of the sites, we used the value of the intersecting grid cell in the N320 grid without interpolation.

For the comparison with CERES, we constructed a top-down ERA5 LCC intended to approximate the ISCCP low-cloud definition ($\mathrm{CTP} > 680$ hPa) more closely. The non-obscured top-down LCC comparable to that of CERES was obtained by applying the overlap model cumulatively first over the whole column top-down and then for the second time only for the upper $\mathrm{CTP} < 680$ hPa part of the column, computing the final unobstructed fraction as

$$f_{\mathrm{low|visible}} = \frac{f_{\mathrm{total}} - f_{\mathrm{above\ low}}}{1 - f_{\mathrm{above\ low}}}, \tag{5}$$

where f_{total} is the column total fractional cloud cover and $f_{\mathrm{above\ low}}$ is the fractional cover for $\mathrm{CTP} < 680$ hPa. We refer to this product as ERA5/CTP for the remainder of the paper.

4.4 Trend analysis

We analysed the LCC trends using the Mann-Kendall test to find statistical significance of the possible trends, and the Theil-Sen estimator to quantify trend magnitude [92; 93; 94; 95]. The choice of methodology was motivated by the following key factors: both the Mann-Kendall test and Theil-Sen estimator are robust to outliers and high-leverage observations, as they are based on rank statistics and median slopes rather than means, making them less sensitive to extreme values or influential data points (such as those near the endpoints of the time series) compared with, e.g. ordinary least squares regression. These properties focus our estimates on underlying consistent trends rather than isolated one-off outliers, whether arising from real events (e.g. highly anomalous weather) or measurement artefacts (e.g. instrument malfunction). Furthermore, as a non-parametric framework, the Mann-Kendall test does not require assumptions regarding the underlying data distribution, which is advantageous for cloud cover records that are not normally distributed at sub-annual granularities. Therefore, the need for strong temporal averaging (e.g. into annual means) that would otherwise reduce statistical power due to smaller sample sizes is avoided. The Mann-Kendall test and Theil-Sen estimator are well-established and widely used for trend analysis of geoscientific time series [96; 97; 98; 99].

The Theil-Sen estimator is defined as the median of the pairwise slopes between observations. In the present application, however, not all pairwise comparisons are appropriate. Cloud cover may exhibit a strong seasonal cycle, such that slopes formed between observations from different meteorological seasons may be dominated by seasonal differences, masking the underlying long-term trend. Furthermore, in the case of the ALCs, observations originate from different instruments with distinct retrieval characteristics, and measurements from different instruments may thus differ by an offset. An offset, if present, would introduce bias in the pairwise slopes computed from cross-instrument observation pairs, whereas within-instrument slopes remain invariant to such offsets. In most cases, the overlap of ALC records from multiple instruments are insufficient to reliably determine the offset.

To account for these effects, we adopted the seasonally stratified Mann–Kendall approach of Hirsch et al.[96], using the four meteorological seasons (December–February DJF, March–May MAM, June–August JJA, and September–November SON) as the strata. Consequently, pairwise comparisons were restricted to observations within the same season. For the ALC observations, the estimator was further restricted to within-instrument comparisons, following Baumdicker et al.[100]. The trend estimate was therefore computed as

$$\hat{\beta} = \mathrm{median}\left\{ \frac{y_j - y_i}{t_j - t_i} \,:\, j > i,\ s_i = s_j,\ g_i = g_j \right\}, \tag{6}$$

where s_i and g_i denote the meteorological season and instrument associated with observation i, respectively. For CERES and ERA5, all observations were treated as belonging to a single instrument, such that only the seasonal restriction was applied.

Confidence distributions for the Theil-Sen trends were obtained by repeatedly inverting the asymptotic Mann-Kendall test over a dense grid of confidence levels. For each confidence level, the variance of the Mann-Kendall statistic (S) under the usual normal approximation was used to determine the corresponding lower and upper order statistics of the sorted admissible pairwise slopes following Sen[94] and Gilbert et al.[97]. Repeating this procedure over a dense grid of confidence levels yields a discrete approximation to the quantile function of the confidence distribution, represented numerically by N_q equally probable quantiles. We set $N_q = 10001$, for which the discretization error was negligible. Confidence intervals at arbitrary confidence levels were obtained directly from the corresponding quantiles of the confidence distribution. In the grouped ALC setting, the confidence distribution was constructed consistently with the restricted Theil-Sen estimator described above: only within-instrument pairs were included in the slope sample, the S, and its variance. Thus, both the trend estimate and its uncertainty were based on exactly the same admissible comparisons. The stratification of the estimator, although necessary to limit biases, greatly limits the number of admissible pairwise comparisons, thus widening the trend confidence distributions. This is especially the case for ALC estimates from sites where the record consists of two or more instruments.

The final joint trend across all study sites was estimated using a Monte Carlo approach based on the individual trend confidence distributions. For each realisation, one trend value was sampled from the confidence distribution of each site, and their mean was calculated. Repeated application of this procedure yielded empirical distributions of the joint trends, from which reported joint means and reported standard errors were obtained. Equal weighting was used to give sites with different levels of trend uncertainty equal weight on the joint trend.

For most sites, cloud fractions were averaged to three-day periods prior to trend estimation. Based on sensitivity tests, the three-day averaging window was the shortest interval for which the distributions of pairwise slopes became sufficiently smooth to derive stable trend estimates and associated confidence distributions. Compared with daily averages, three-day averaging greatly reduces the occurrence of tied pairwise comparisons, while avoiding the substantial reduction in sample size associated with longer averaging periods. For sites associated with a low climatological LCC, Granada and Lamont, a longer averaging time of one month was used.

Despite averaging, the resulting anomaly time series may be autocorrelated in time, primarily due to the persistence of synoptic-scale weather patterns and their associated impacts on cloud cover. This residual autocorrelation can inflate type I error in the Mann–Kendall test, leading to overconfident uncertainty estimates and overly concentrated confidence distributions. Conversely, directly removing lag-1 autocorrelation could increase type II error in uncertainty estimation, resulting in artificial widening of the confidence distributions. To address both error types, we adopted the '3PW' prewhitening algorithm by Collaud Coen et al.[101], which combines several prewhitening methods to limit both type I and II errors compared with application of the individual methods separately.

To ensure comparability of the datasets, we limited the data from each site to the data coverage of the combined ALC or CERES dataset (intersection). Hence, the earliest possible date included in the trend analysis is 1 March 2000, marking the beginning of the CERES SYN1deg record. However, for most of the sites ALC data coverage was more limiting as reported in Table 1. All valid data within the coverage period was included in the trend estimation, i.e. gaps in ALC coverage were not excluded from CERES or ERA5 trend estimation.

Beyond the annual trends, we also computed trends segmented by the meteorological seasons following Hirsch et al.[96] and Collaud Coen et al.[101]. Although seasonal segmentation decreases the number of data points available for the trend estimation by a factor of four, the seasonal trends are an important indication of potential seasonal heterogeneity of the annual trends, which may reveal underlying factors leading to differences in the annual trends. Furthermore, presence of strong seasonal heterogeneity in the trends may lead to decrease in the statistical reliability of the annual trend estimates and associated uncertainty [97; 101].

Data availability

The ACTRIS Cloudnet data are publicly available from the ACTRIS Data Centre at `https://cloudnet.fmi.fi`. The ARM data is publicly available from the ARM User Facility at `https://www.arm.gov/data`. The ERA5 reanalysis data is available on Copernicus Climate Change Service (C3S) Climate Data Store (CDS) at `https://doi.org/10.24381/cds.143582cf` [102].

For the final publication, the processed instantaneous and aggregated ALC, ERA5, and CERES data will be stored persistently in a data repository under Creative Commons Attribution 4.0 (CC-BY) license.

Acknowledgements

The authors would like to thank Ewan O'Connor for his support with the ALC processing and for providing ALC data from the Finnish sites. We acknowledge Aerosol, Clouds and Trace Gases Research Infrastructure (ACTRIS), U.S. Department of Energy Atmospheric Radiation Measurement (ARM), Finnish Meteorological Institute (FMI), Swiss Federal Office of Meteorology and Climatology (MeteoSwiss), Royal Netherlands Meteorological Institute (KNMI), New Zealand National Institute of Water and Atmospheric Science (NIWA), Norwegian Meteorological Institute (MET Norway), and UK Science and Technology Facilities Council (STFC) for providing the ALC data sets used in the study. The authors would also like to thank Marijn de Haij, Richard Querel, and Maxime Hervo for providing ALC data from Cabauw, Lauder, and Payerne respectively.

This study was conducted as part of the Horizon Europe project UrbanAIR and has received funding from the Swiss State Secretariat for Education, Research and Innovation.

Author contributions

Conceptualisation: S.K., A.M. Methodology: S.K., S.R. Investigation: S.K. Visualisation: S.K. Writing - original draft: S.K. Writing - review & editing: S.K., S.R., A.M.

Competing interests

The authors declare no competing interests.

References

[1] Stephens, G. L. Cloud feedbacks in the climate system: A critical review. *Journal of Climate* **18**, 237–273 (2005).

[2] Wood, R. Stratocumulus clouds. *Monthly Weather Review* **140**, 2373–2423 (2012).

[3] Zelinka, M. D. *et al.* Contributions of different cloud types to feedbacks and rapid adjustments in CMIP5. *Journal of Climate* **26**, 5007–5027 (2013).

[4] Zelinka, M. D. *et al.* Causes of higher climate sensitivity in CMIP6 models. *Geophysical Research Letters* **47**, e2019GL085782 (2020).

[5] Sherwood, S. C. *et al.* An assessment of Earth's climate sensitivity using multiple lines of evidence. *Reviews of Geophysics* **58**, e2019RG000678 (2020).

[6] Goessling, H. F., Rackow, T. & Jung, T. Recent global temperature surge intensified by record-low planetary albedo. *Science* **387**, 68–73 (2025).

[7] Ceppi, P. *et al.* Emerging low-cloud feedback and adjustment in global satellite observations. *Atmospheric Chemistry and Physics* **26**, 4153–4171 (2026).

[8] Andrews, T., Gregory, J. M., Forster, P. M. & Webb, M. J. Cloud adjustment and its role in CO2 radiative forcing and climate sensitivity: A review. *Surveys in Geophysics* **33**, 619–635 (2012).

[9] Qu, X., Hall, A., Klein, S. A. & Caldwell, P. M. On the spread of changes in marine low cloud cover in climate model simulations of the 21st century. *Climate Dynamics* **42**, 2603–2626 (2014).

[10] Scott, R. C. *et al.* Observed sensitivity of low-cloud radiative effects to meteorological perturbations over the global oceans. *Journal of Climate* **33**, 7717–7734 (2020).

[11] Ceppi, P., Brient, F., Zelinka, M. D. & Hartmann, D. L. Cloud feedback mechanisms and their representation in global climate models. *WIREs Climate Change* **8**, e465 (2017).

[12] Klein, S. A., Hall, A., Norris, J. R. & Pincus, R. Low-cloud feedbacks from cloud-controlling factors: A review. *Surveys in Geophysics* **38**, 1307–1329 (2017).

[13] Liu, H., Koren, I., Altaratz, O. & Chekroun, M. D. Opposing trends of cloud coverage over land and ocean under global warming. *Atmospheric Chemistry and Physics* **23**, 6559–6569 (2023).

[14] Dong, B., Sutton, R. T. & Wilcox, L. J. Decadal trends in surface solar radiation and cloud cover over the North Atlantic sector during the last four decades: Drivers and physical processes. *Climate Dynamics* **60**, 2533–2546 (2023).

[15] Gregory, J. & Webb, M. Tropospheric adjustment induces a cloud component in CO2 forcing. *Journal of Climate* **21**, 58 – 71 (2008).

[16] Doutriaux-Boucher, M., Webb, M. J., Gregory, J. M. & Boucher, O. Carbon dioxide induced stomatal closure increases radiative forcing via a rapid reduction in low cloud. *Geophysical Research Letters* **36** (2009).

[17] Tselioudis, G., Remillard, J., Jakob, C. & Rossow, W. B. Contraction of the world's storm-cloud zones the primary contributor to the 21st century increase in the Earth's sunlight absorption. *Geophysical Research Letters* **52**, e2025GL114882 (2025).

[18] Hodnebrog, Ø. *et al.* Recent reductions in aerosol emissions have increased Earth's energy imbalance. *Communications Earth & Environment* **5**, 166 (2024).

[19] Gettelman, A. *et al.* Has reducing ship emissions brought forward global warming? *Geophysical Research Letters* **51**, e2024GL109077 (2024).

[20] von Salzen, K. *et al.* Reduced aerosol pollution diminished cloud reflectivity over the North Atlantic and Northeast Pacific. *Nature Communications* **16**, 9433 (2025).

[21] Talvinen, S. *et al.* Beyond cloud cover: Low- and high-altitude clouds have distinct impacts on tree sap flow and transpiration. *Agricultural and Forest Meteorology* **384**, 111182 (2026).

[22] Stephens, G. L. *et al.* The changing nature of Earth's reflected sunlight. *Proceedings of the Royal Society A: Mathematical, Physical and Engineering Sciences* **478**, 20220053 (2022).

[23] Kramer, R. J. *et al.* Observational evidence of increasing global radiative forcing. *Geophysical Research Letters* **48**, e2020GL091585 (2021).

[24] Zelinka, M. D., Klein, S. A. & Hartmann, D. L. Computing and partitioning cloud feedbacks using cloud property histograms. part II: Attribution to changes in cloud amount, altitude, and optical depth. *Journal of Climate* **25**, 3736–3754 (2012).

[25] Loeb, N. G. *et al.* Observational assessment of changes in Earth's energy imbalance since 2000. *Surveys in Geophysics* **45**, 1757–1783 (2024).

[26] Wielicki, B. A. *et al.* Clouds and the earth's radiant energy system (ceres): An earth observing system experiment. *Bulletin of the American Meteorological Society* **77**, 853 – 868 (1996). URL `https://journals.ametsoc.org/view/journals/bams/77/5/1520-0477_1996_077_0853_catere_2_0_co_2.xml`.

[27] Devasthale, A. & Karlsson, K.-G. Decadal stability and trends in the global cloud amount and cloud top temperature in the satellite-based climate data records. *Remote Sensing* **15** (2023).

[28] Ceppi, P., Myers, T. A., Nowack, P., Wall, C. J. & Zelinka, M. D. Implications of a pervasive climate model bias for low-cloud feedback. *Geophysical Research Letters* **51**, e2024GL110525 (2024).

[29] Yuan, T., Oreopoulos, L., Platnick, S. E. & Meyer, K. Observations of local positive low cloud feedback patterns and their role in internal variability and climate sensitivity. *Geophysical Research Letters* **45**, 4438–4445 (2018).

[30] Bender, F. A.-M., Engström, A., Wood, R. & Charlson, R. J. Evaluation of hemispheric asymmetries in marine cloud radiative properties. *Journal of Climate* **30**, 4131 – 4147 (2017).

[31] Norris, J. R. What can cloud observations tell us about climate variability? *Space Science Reviews* **94**, 375–380 (2000).

[32] Evan, A. T., Heidinger, A. K. & Vimont, D. J. Arguments against a physical long-term trend in global ISCCP cloud amounts. *Geophysical Research Letters* **34** (2007).

[33] Norris, J. R. & Evan, A. T. Empirical removal of artifacts from the ISCCP and PATMOS-x satellite cloud records. *Journal of Atmospheric and Oceanic Technology* **32**, 691 – 702 (2015).

[34] Norris, J. R. *et al.* Evidence for climate change in the satellite cloud record. *Nature* **536**, 72–75 (2016).

[35] Hersbach, H. *et al.* The ERA5 global reanalysis. *Quarterly Journal of the Royal Meteorological Society* **146**, 1999–2049 (2020).

[36] Illingworth, A. J. *et al.* Cloudnet: Continuous evaluation of cloud profiles in seven operational models using ground-based observations. *Bulletin of the American Meteorological Society* **88**, 883 – 898 (2007).

[37] Zelinka, M. D., Klein, S. A. & Hartmann, D. L. Computing and partitioning cloud feedbacks using cloud property histograms. part I: Cloud radiative kernels. *Journal of Climate* **25**, 3715–3735 (2012).

[38] Pincus, R., Platnick, S., Ackerman, S. A., Hemler, R. S. & Hofmann, R. J. P. Reconciling simulated and observed views of clouds: MODIS, ISCCP, and the limits of instrument simulators. *Journal of Climate* **25**, 4699–4720 (2012).

[39] Marchand, R., Ackerman, T., Smyth, M. & Rossow, W. B. A review of cloud top height and optical depth histograms from MISR, ISCCP, and MODIS. *Journal of Geophysical Research: Atmospheres* **115** (2010).

[40] Stubenrauch, C. J. *et al.* Assessment of global cloud datasets from satellites: Project and database initiated by the GEWEX radiation panel. *Bulletin of the American Meteorological Society* **94**, 1031–1049 (2013).

[41] Marchand, R. ARM and satellite cloud validation. *Meteorological Monographs* **57**, 30.1–30.11 (2016).

[42] de Haij, M. J., Apituley, A., Koetse, W. & Bloemink, H. I. *Transition towards a new ceilometer network in the Netherlands: Challenges and experiences* (World Meteorological Organization, 2016). URL `https://www.knmi.nl/research/publications/transition-towards-a-new-ceilometer-network-in-the-netherlands-challenges-and-experiences`.

[43] de Haij, M. KNMI CHM15k lidar data from Cabauw (2026). URL `https://hdl.handle.net/21.12132/3.c07f533cd86041f1`.

[44] Science and Technology Facilities Council, Chilbolton Facility for Atmospheric and Radio Research & Agnew, J. 905 nm Vaisala CT75K lidar ceilometer data from the Chilbolton Facility for Atmospheric and Radio Research (CFARR) site, Hampshire, England, 1996–2013 (2015).

[45] Walden, C. UKRI CL51 lidar data from Chilbolton (2026). URL https://hdl.handle.net/21.12132/3.1ca2b7d6323f486b.

[46] MET Norway. MET Norway CHM15k lidar data (2026). URL https://thredds.met.no/thredds/catalog/remotesensingceilometer/catalog.html.

[47] Zhang, D., Morris, V. & Ermold, B. Ceilometer (CEIL10M & CEIL), 1997-09-14 to 2025-12-31, Eastern North Atlantic (ENA), Graciosa Island, Azores, Portugal (C1), North Slope Alaska (NSA), Central Facility, Barrow AK (C1), and Southern Great Plains (SGP), Central Facility, Lamont, OK (C1) (2026).

[48] Cazorla Cabrera, A. UGR CHM15k lidar data from Granada (2026). URL https://hdl.handle.net/21.12132/3.77a75f3b32294855.

[49] Schween, J. UoC CHM15k lidar data from Jülich (2026). URL https://hdl.handle.net/21.12132/3.324507c6ce8e489c.

[50] Schween, J. UoC CT25k lidar data from Jülich (2026). URL https://hdl.handle.net/21.12132/3.9a9061d587e24dc8.

[51] O'Connor, E. FMI CT25k lidar data from Kenttärova (2026). URL https://hdl.handle.net/21.12132/3.b5b5f67e68324bfe.

[52] O'Connor, E. FMI CL31 lidar data from Kenttärova (2026). URL https://hdl.handle.net/21.12132/3.2a7c4f8b6c1344f3.

[53] Görsdorf, U. DWD lidar data from Lindenberg (2026). URL https://hdl.handle.net/21.12132/3.cdf99c536bd04146.

[54] Kotthaus, S. IPSL CL31 lidar data from Palaiseau (2026). URL https://hdl.handle.net/21.12132/3.627a31d354ea4108.

[55] Kotthaus, S. IPSL CHM15k lidar data from Palaiseau (2026). URL https://hdl.handle.net/21.12132/3.b14e15ec9c9b43fb.

[56] Hervo, M. MeteoSwiss CHM15k lidar data from Payerne (2026). URL https://hdl.handle.net/21.12132/3.5ffe1a5df37145cc.

[57] Komppula, M. FMI CL51 lidar data from Vehmasmäki (2026). URL https://hdl.handle.net/21.12132/3.8761e421c5d3466f.

[58] Devasthale, A. *et al.* Leveraging the satellite-based climate data record clara-a3 to understand the climatic trend regimes relevant for solar energy applications over europe. *Earth System Dynamics* **16**, 1169–1182 (2025). URL https://esd.copernicus.org/articles/16/1169/2025/.

[59] Mitra, A., Ghate, V. & Rutan, D. Comparison of ceres syn1deg radiative fluxes with those derived from observations at the arm ena site. *Journal of Climate* **38**, 6475 – 6491 (2025). URL https://journals.ametsoc.org/view/journals/clim/38/22/JCLI-D-24-0633.1.xml.

[60] Dutta, S. *et al.* The reduction in near-global cloud cover after correcting for biases caused by finite resolution measurements. *Geophysical Research Letters* **47**, e2020GL090313 (2020).

[61] Kuma, P. *et al.* Ship-based lidar evaluation of southern ocean low clouds in the storm-resolving general circulation model icon and the era5 and merra-2 reanalyses. *Journal of Geophysical Research: Atmospheres* **130**, e2024JD043145 (2025).

[62] Ackerman, S. A. *et al.* Cloud detection with MODIS. part II: Validation. *Journal of Atmospheric and Oceanic Technology* **25**, 1073–1086 (2008).

[63] Heese, B., Flentje, H., Althausen, D., Ansmann, A. & Frey, S. Ceilometer lidar comparison: backscatter coefficient retrieval and signal-to-noise ratio determination. *Atmospheric Measurement Techniques* **3**, 1763–1770 (2010). URL https://amt.copernicus.org/articles/3/1763/2010/.

[64] Le, V., O'Connor, E. J., Filioglou, M. & Vakkari, V. Operational performance of the vaisala cl61 ceilometer for atmospheric profiling. *Atmospheric Measurement Techniques* **19**, 4923–4941 (2026). URL https://amt.copernicus.org/articles/19/4923/2026/.

[65] King, M. D., Platnick, S., Menzel, W. P., Ackerman, S. A. & Hubanks, P. A. Spatial and temporal distribution of clouds observed by modis onboard the terra and aqua satellites. *IEEE Transactions on Geoscience and Remote Sensing* **51**, 3826–3852 (2013).

[66] Bromwich, D. H. *et al.* Tropospheric clouds in Antarctica. *Reviews of Geophysics* **50** (2012).

[67] Brunke, M. A., de Szoeke, S. P., Zuidema, P. & Zeng, X. A comparison of ship and satellite measurements of cloud properties with global climate model simulations in the southeast Pacific stratus deck. *Atmospheric Chemistry and Physics* **10**, 6527–6536 (2010).

[68] Ye, J., Liu, L., Shang, Y., Ding, J. & Xie, H. Remote sensing of Arctic marine fog using ship-based ceilometer. *Atmospheric Research* **324**, 108204 (2025).

[69] Hopkin, E., Illingworth, A. J., Charlton-Perez, C., Westbrook, C. D. & Ballard, S. A robust automated technique for operational calibration of ceilometers using the integrated backscatter from totally attenuating liquid clouds. *Atmospheric Measurement Techniques* **12**, 4131–4147 (2019).

[70] Wehr, T. *et al.* The EarthCARE mission – science and system overview. *Atmospheric Measurement Techniques* **16**, 3581–3608 (2023).

[71] Doelling, D. R. *et al.* Geostationary enhanced temporal interpolation for ceres flux products. *Journal of Atmospheric and Oceanic Technology* **30**, 1072 – 1090 (2013). URL `https://journals.ametsoc.org/view/journals/atot/30/6/jtech-d-12-00136_1.xml`.

[72] Doelling, D. R. *et al.* Advances in geostationary-derived longwave fluxes for the ceres synoptic (syn1deg) product. *Journal of Atmospheric and Oceanic Technology* **33**, 503 – 521 (2016). URL `https://journals.ametsoc.org/view/journals/atot/33/3/jtech-d-15-0147_1.xml`.

[73] Doelling, D., Haney, C., Bhatt, R., Scarino, B. & Gopalan, A. Geostationary visible imager calibration for the ceres syn1deg edition 4 product. *Remote Sensing* **10** (2018). URL `https://www.mdpi.com/2072-4292/10/2/288`.

[74] Menzel, W. P. *et al.* MODIS global cloud-top pressure and amount estimation: Algorithm description and results. *Journal of Applied Meteorology and Climatology* **47**, 1175–1198 (2008).

[75] Twedt, K., Xiong, X., Geng, X., Wilson, T. & Mu, Q. *Impact of satellite orbit drift on MODIS Earth scene observations used in calibration of the reflective solar bands*, Vol. 12685, 158–167 (SPIE, 2023).

[76] Maddux, B. C., Ackerman, S. A. & Platnick, S. Viewing geometry dependencies in MODIS cloud products. *Journal of Atmospheric and Oceanic Technology* **27**, 1519–1528 (2010).

[77] Laj, P. *et al.* Aerosol, Clouds and Trace Gases Research Infrastructure (ACTRIS): The European research infrastructure supporting atmospheric science. *Bulletin of the American Meteorological Society* **105**, E1098 – E1136 (2024).

[78] Stokes, G. M. & Schwartz, S. E. The Atmospheric Radiation Measurement (ARM) program: Programmatic background and design of the cloud and radiation test bed. *Bulletin of the American Meteorological Society* **75**, 1201 – 1222 (1994).

[79] Beck, H. E. *et al.* Present and future Köppen-Geiger climate classification maps at 1-km resolution. *Scientific Data* **5**, 180214 (2018).

[80] Tuononen, M., O'Connor, E. J. & Sinclair, V. A. Evaluating solar radiation forecast uncertainty. *Atmospheric Chemistry and Physics* **19**, 1985–2000 (2019).

[81] de Haij, M. J., Wauben, W. M. F. & Klein Baltink, H. Continuous mixing layer height determination using the LD-40 ceilometer: A feasibility study. KNMI Scientific Report WR-07-01, Royal Netherlands Meteorological Institute (KNMI), De Bilt, The Netherlands (2007). URL `https://www.knmi.nl/kennis-en-datacentrum/publicatie/continuous-mixing-layer-height-determination-using-the-ld-40-ceilometer-a-feasibility-study`.

[82] Tukiainen, S., O'Connor, E. & Korpinen, A. CloudnetPy: A Python package for processing cloud remote sensing data. *Journal of Open Source Software* **5**, 2123 (2020).

[83] Loeb, N. G. *et al.* Clouds and the earth's radiant energy system (ceres) energy balanced and filled (ebaf) top-of-atmosphere (toa) edition-4.0 data product. *Journal of Climate* **31**, 895 – 918 (2018). URL `https://journals.ametsoc.org/view/journals/clim/31/2/jcli-d-17-0208.1.xml`.

[84] Kato, S. *et al.* Surface irradiances of edition 4.0 clouds and the earth's radiant energy system (ceres) energy balanced and filled (ebaf) data product. *Journal of Climate* **31**, 4501 – 4527 (2018). URL `https://journals.ametsoc.org/view/journals/clim/31/11/jcli-d-17-0523.1.xml`.

[85] Schiffer, R. A. & Rossow, W. B. The International Satellite Cloud Climatology Project (ISCCP): The first project of the World Climate Research Programme. *Bulletin of the American Meteorological Society* **64**, 779 – 784 (1983).

[86] Rossow, W. B. & Schiffer, R. A. Advances in understanding clouds from ISCCP. *Bulletin of the American Meteorological Society* **80**, 2261 – 2288 (1999).

[87] Myers, T. A. *et al.* Observational constraints on low cloud feedback reduce uncertainty of climate sensitivity. *Nature Climate Change* **11**, 501–507 (2021).

[88] Zelinka, M. D. *et al.* Recent cloud trends and extremes reaffirm established bounds on cloud feedback and aerosol-cloud interactions. *Communications Earth & Environment* (2026).

[89] Hogan, R. J. & Illingworth, A. J. Deriving cloud overlap statistics from radar. *Quarterly Journal of the Royal Meteorological Society* **126**, 2903–2909 (2000).

[90] Räisänen, P., Barker, H. W., Khairoutdinov, M. F., Li, J. & Randall, D. A. Stochastic generation of subgrid-scale cloudy columns for large-scale models. *Quarterly Journal of the Royal Meteorological Society* **130**, 2047–2067 (2004).

[91] ECMWF. in *IFS documentation CY41r2 - part IV: Physical processes* 4 (ECMWF, 2016).

[92] Mann, H. B. Nonparametric tests against trend. *Econometrica* **13**, 245–259 (1945).

[93] Theil, H. A rank-invariant method of linear and polynomial regression analysis. *Nederl. Akad. Wetensch., Proc.* **53**, 386–392 (1950).

[94] Sen, P. K. Estimates of the regression coefficient based on Kendall's tau. *Journal of the American Statistical Association* **63**, 1379–1389 (1968).

[95] Kendall, M. G. *Rank correlation methods* 4th ed., 2d impression edn (Griffin, 1975).

[96] Hirsch, R. M., Slack, J. R. & Smith, R. A. Techniques of trend analysis for monthly water quality data. *Water Resources Research* **18**, 107–121 (1982).

[97] Gilbert, R. O. in *Statistical methods for environmental pollution monitoring* PNL–4660 (John Wiley & Sons, 1987).

[98] Hamed, K. H. Trend detection in hydrologic data: The Mann–Kendall trend test under the scaling hypothesis. *Journal of Hydrology* **349**, 350–363 (2008).

[99] Zaman, S. M. & Jha, M. K. Seasonal and annual precipitation time series trend analysis in North Carolina, United States. *Atmospheric Research* **137**, 183–194 (2014).

[100] Baumdicker, F. & Hölker, U. Method comparison with repeated measurements — Passing–Bablok regression for grouped data with errors in both variables. *Statistics & Probability Letters* **164**, 108801 (2020).

[101] Collaud Coen, M. *et al.* Effects of the prewhitening method, the time granularity, and the time segmentation on the Mann–Kendall trend detection and the associated Sen's slope. *Atmospheric Measurement Techniques* **13**, 6945–6964 (2020).

[102] Hersbach, H. *et al.* Complete ERA5 from 1940: Fifth generation of ECMWF atmospheric reanalyses of the global climate (2017).